

Water Oxidation

International Edition: DOI: 10.1002/anie.201601943
German Edition: DOI: 10.1002/ange.201601943

Water Oxidation by Ruthenium Complexes Incorporating Multifunctional Bipyridyl Diphosphonate Ligands

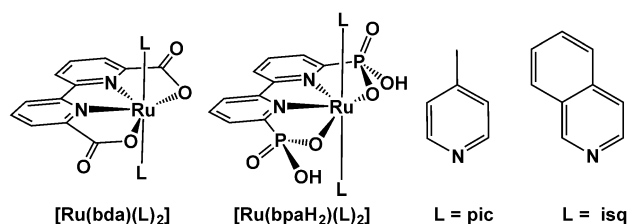
Yan Xie, David W. Shaffer, Anna Lewandowska-Andralojc, David J. Szalda, and Javier J. Concepcion*

Abstract: We describe herein the synthesis and characterization of ruthenium complexes with multifunctional bipyridyl diphosphonate ligands as well as initial water oxidation studies. In these complexes, the phosphonate groups provide redox-potential leveling through charge compensation and σ donation to allow facile access to high oxidation states. These complexes display unique pH-dependent electrochemistry associated with deprotonation of the phosphonic acid groups. The position of these groups allows them to shuttle protons in and out of the catalytic site and reduce activation barriers. A mechanism for water oxidation by these catalysts is proposed on the basis of experimental results and DFT calculations. The unprecedented attack of water at a neutral six-coordinate $[Ru^{IV}]$ center to yield an anionic seven-coordinate $[Ru^{IV}-OH]^-$ intermediate is one of the key steps of a single-site mechanism in which all species are anionic or neutral. These complexes are among the fastest single-site catalysts reported to date.

The oxidation of water to oxygen provides the redox equivalents and protons required to store solar energy in chemical bonds in natural photosynthesis.^[1] This energy is used by living organisms in respiration, reproduction, and growth. For decades, scientists have tried to emulate photosynthesis to store solar energy as useful fuels. Owing to demands imposed by unprecedented levels of worldwide energy consumption and changes to the global climate, this goal has become more than a scientific curiosity. Reaching this milestone requires the development of water oxidation catalysts capable of promoting this half reaction efficiently, at high rates, and for long periods of time.

Known molecular catalysts for water oxidation include both multinuclear^[2] and mononuclear complexes;^[3] single-site catalysts are a particular case of each of these types.^[4] Molecular systems are attractive because of the potential to tune their properties by varying the ligand and/or metal.^[5]

Among these systems, ruthenium complexes incorporating 2,2'-bipyridine-6,6'-dicarboxylic acid (bdaH₂; Scheme 1) have



Scheme 1. Structures of $[Ru^{II}(bda)(L)_2]$ (L is 4-picoline, pic, or isoquinoline, isq) and $[Ru^{II}(bpaH_2)(L)_2]$.

drawn significant attention because of their impressive water oxidation rates with cerium(IV) as a sacrificial oxidant.^[3a,b] The carboxylate groups in the bda²⁻ ligand increase the electron density on the Ru center, thus enabling easier access to high oxidation states. They can also inhibit anation by providing charge compensation in high oxidation state intermediates.^[6] The catalytic activity of $[Ru(bda)(L)_2]$ catalysts can be enhanced by the addition of bases.^[7] This behavior is also known for other catalysts and originates from the involvement of proton transfer in the rate-limiting step.^[8] However, the $[Ru(bda)(L)_2]$ family of catalysts follows a bimolecular pathway for O–O bond formation. As a result, rates of site-isolated catalysts for water oxidation on metal-oxide surfaces are orders of magnitude lower than for freely diffusing catalysts in solution.^[6]

We report herein ruthenium complexes with the ligand 2,2'-bipyridine-6,6'-diphosphonic acid (bpaH₄; Scheme 1). Initial studies show distinct electrochemical behavior associated with proton-coupled electron transfer (PCET) owing to deprotonation of the phosphonic acid groups, thus enabling easy access to high oxidation states. Besides providing effective electron donation and charge compensation similar to the bda²⁻ ligand, the bpaH₂²⁻ ligand introduces three key functionalities: The water solubility and stability of the complexes are increased; the PCET nature of the oxidations (see below) leads to substantially lower oxidation potentials; and the deprotonated phosphonate bases can facilitate proton transfer at the catalytic site. These compounds display excellent activity towards catalytic water oxidation and follow a single-site mechanism,^[4] although with some unique variations. The activity of single-site catalysts is retained when site-isolated on metal-oxide surfaces, a desirable property for true device configurations.^[4a,6]

[*] Y. Xie, Dr. D. W. Shaffer, Dr. A. Lewandowska-Andralojc, Dr. J. J. Concepcion
Chemistry Division, Brookhaven National Laboratory
Upton, NY 11973-5000 (USA)
E-mail: jconcepc@bnl.gov
Dr. D. J. Szalda
Department of Natural Sciences, Baruch College, CUNY
New York, NY 10010 (USA)
Dr. A. Lewandowska-Andralojc
Present address: Faculty of Chemistry, Adam Mickiewicz University
Umultowska 89b, 61614, Poznan (Poland)

Supporting information for this article, including synthetic procedures and characterization details, can be found under: <http://dx.doi.org/10.1002/anie.201601943>.

Our synthetic strategy to prepare the $[\text{Ru}^{\text{II}}(\text{bpaH}_2)(\text{L})_2]$ complexes as well as their $[\text{Ru}^{\text{II}}(\text{bpaEt}_2)(\text{L})_2]$ aprotic analogues is shown in Scheme S1 in the Supporting Information. We used the aprotic $[\text{Ru}^{\text{II}}(\text{bpaEt}_2)(\text{L})_2]$ complexes for comparison with their $[\text{Ru}^{\text{II}}(\text{bpaH}_2)(\text{L})_2]$ protic analogues to study the influence on catalytic activity of PCET, the overall charge, and the presence of basic groups in close proximity to the active site.

Figure 1 (left) shows the X-ray crystal structure of the $[\text{Ru}^{\text{III}}(\text{bpa})(\text{pic})_2]^-$ anion obtained by aerobic oxidation of $[\text{Ru}^{\text{II}}(\text{bpaH}_2)(\text{pic})_2]$. It shares a $[\text{Mg}(\text{OH})_2]^{2+}$ counterion with another $[\text{Ru}^{\text{III}}(\text{bpa})(\text{pic})_2]^-$ anion in the crystal lattice, and it is connected to a network of water molecules through hydrogen-bonding interactions (see Figure S25 in the Supporting Information). The structure resembles those of $[\text{Ru}^{\text{III}}(\text{bda})(\text{pic})_2]^+$ and $[\text{Ru}^{\text{III}}(\text{bda})(\text{isq})_2]^+$ with respect to bond distances (see Table S1),^[6] but the O4-Ru-O1 angle is significantly smaller for $[\text{Ru}^{\text{III}}(\text{bpa})(\text{pic})_2]^-$ as compared to $[\text{Ru}^{\text{III}}(\text{bda})(\text{pic})_2]^+$ and $[\text{Ru}^{\text{III}}(\text{bda})(\text{isq})_2]^+$ (112.1 vs. 126.4 and 126.0°, respectively).

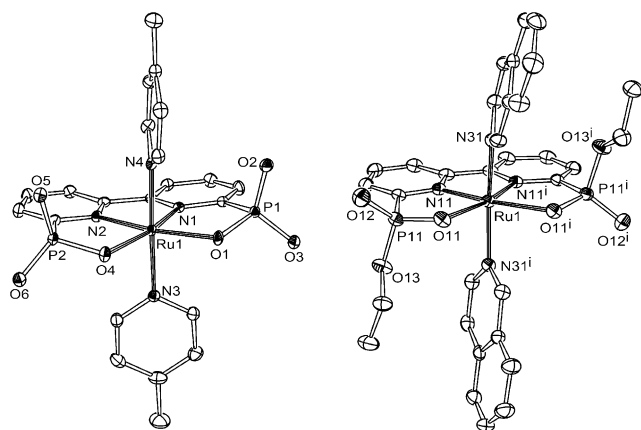


Figure 1. ORTEP drawing of the X-ray crystal structures of the $[\text{Ru}^{\text{III}}(\text{bpa})(\text{pic})_2]^-$ anion (left) and one of the isomers of $[\text{Ru}^{\text{II}}(\text{bpaEt}_2)(\text{isq})_2]$ (right). The ellipsoid probability is 50%.

$[\text{Ru}^{\text{II}}(\text{bpaEt}_2)(\text{pic})_2]$ and $[\text{Ru}^{\text{II}}(\text{bpaEt}_2)(\text{isq})_2]$ were obtained as equimolar mixtures of two isomers with different arrangements of the ethyl groups, as determined by ^1H NMR spectroscopy (see Figures S6 and S7). Figure 1 (right) shows the X-ray crystal structure of one of the two isomers of $[\text{Ru}^{\text{II}}(\text{bpaEt}_2)(\text{isq})_2]$, in which the two ethyl groups are on opposite sides of the equatorial bpa ligand. On the other hand, in the opposite isomer of $[\text{Ru}^{\text{II}}(\text{bpaEt}_2)(\text{pic})_2]$ (shown in Figure S8), the two ethyl groups are on the same side. The coordination environment around Ru for $[\text{Ru}^{\text{II}}(\text{bpaEt}_2)(\text{isq})_2]$ is similar to that of $[\text{Ru}^{\text{III}}(\text{bpa})(\text{pic})_2]^-$ but with longer Ru–O bond distances (2.173 vs. 2.034 Å) and shorter Ru–N_{bpy} bond distances (1.951 vs. 1.998 Å; bpy is 2,2'-bipyridyl). These differences are in line with the difference in the oxidation state of Ru in the two complexes.

Significant insight can be gained from comparing the electrochemistry of $[\text{Ru}^{\text{II}}(\text{bpaH}_2)(\text{L})_2]$ and $[\text{Ru}^{\text{II}}(\text{bpaEt}_2)(\text{L})_2]$. Cyclic voltammograms (CVs) for $[\text{Ru}^{\text{II}}(\text{bpaH}_2)(\text{pic})_2]$ and $[\text{Ru}^{\text{II}}(\text{bpaEt}_2)(\text{pic})_2]$ at pH 1.0 and 2.9 with 10% CH_3CN

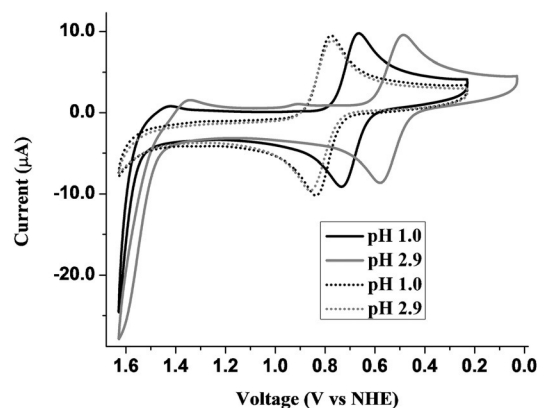


Figure 2. CVs for 1.0 mM $[\text{Ru}^{\text{II}}(\text{bpaH}_2)(\text{pic})_2]$ (solid lines) and $[\text{Ru}^{\text{II}}(\text{bpaEt}_2)(\text{pic})_2]$ (dashed lines) at pH 1.0 and 2.9 (100 mVs^{-1} , glassy carbon electrode, in 1:9 $\text{CH}_3\text{CN}/\text{H}_2\text{O}$).

are shown in Figure 2 (see Figure S9 for cyclic and square-wave voltammograms for these two complexes at various pH values). They both display a reversible one-electron $\text{Ru}^{\text{III/II}}$ couple (+0.68 and +0.80 V, respectively, at pH 1.0; all redox potentials presented herein are versus the normal hydrogen electrode, NHE). This couple is pH-dependent for $[\text{Ru}^{\text{II}}(\text{bpaH}_2)(\text{pic})_2]$ but not for $[\text{Ru}^{\text{II}}(\text{bpaEt}_2)(\text{pic})_2]$, a clear indication of the involvement of the phosphonic acid groups in the pH-dependence for the former. Furthermore, $[\text{Ru}^{\text{II}}(\text{bpaH}_2)(\text{pic})_2]$ displays a $\text{Ru}^{\text{IV/III}}$ couple just before the onset of a water oxidation catalysis wave. The absence of these features for $[\text{Ru}^{\text{II}}(\text{bpaEt}_2)(\text{pic})_2]$ highlights the importance of the electron-donation and additional charge-compensation ability of deprotonated phosphonate groups for reaching the high oxidation states at Ru required for water oxidation catalysis.

The pH-dependence of the electrochemistry for $[\text{Ru}^{\text{II}}(\text{bpaH}_2)(\text{L})_2]$ was studied in detail. CVs for $[\text{Ru}^{\text{II}}(\text{bpaH}_2)(\text{pic})_2]$ in aqueous solutions at different pH values are shown in Figure 3 (see Figure S10 for similar data for $[\text{Ru}^{\text{II}}(\text{bpaH}_2)(\text{isq})_2]$). Both $[\text{Ru}^{\text{II}}(\text{bpaH}_2)(\text{pic})_2]$ and $[\text{Ru}^{\text{II}}(\text{bpaH}_2)(\text{isq})_2]$ display a reversible one-electron, pH-dependent $\text{Ru}^{\text{III/II}}$ couple. In 1.0 M HClO_4 , the $E_{1/2}$ value for this couple is +0.71 V for $[\text{Ru}^{\text{II}}(\text{bpaH}_2)(\text{pic})_2]$ and +0.74 V for $[\text{Ru}^{\text{II}}(\text{bpaH}_2)(\text{isq})_2]$. The redox potential calculated by using DFT

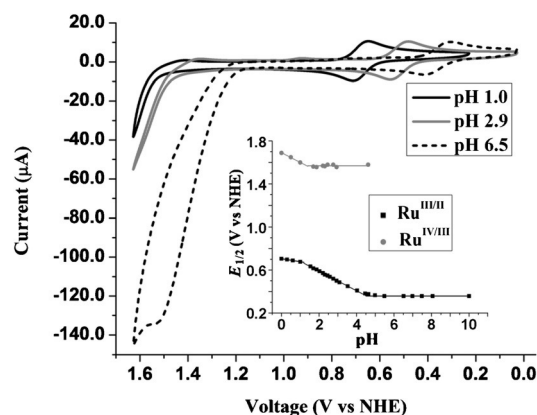
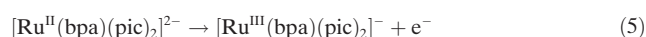
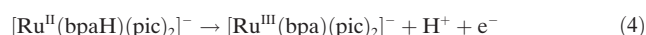
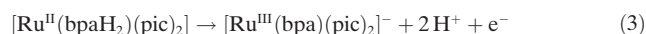
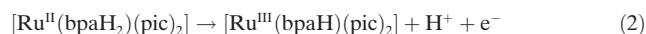
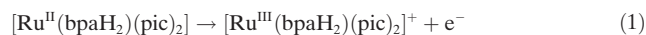


Figure 3. CVs for 1.0 mM $[\text{Ru}^{\text{II}}(\text{bpaH}_2)(\text{pic})_2]$ at various pH values. Inset: Pourbaix diagram for $[\text{Ru}^{\text{II}}(\text{bpaH}_2)(\text{pic})_2]$.

for the oxidation of $[\text{Ru}^{\text{II}}(\text{bpaH}_2)(\text{pic})_2]$ to $[\text{Ru}^{\text{III}}(\text{bpaH}_2)(\text{pic})_2]^+$ is 0.72 V (see the Supporting Information for calculation details), in excellent agreement with the experimental data. At pH 6.5 (0.1M phosphate buffer solution), these couples move to +0.36 and +0.39 V, respectively. The one-electron nature of the $\text{Ru}^{\text{III/II}}$ couple was verified by controlled potential electrolysis at 0.95 V (pH 1.0) and 0.7 V (pH 6.7; see Figure S11).

A second one-electron couple is discernible from pH 0 to approximately pH 4.7 at much higher potentials than the $\text{Ru}^{\text{III/II}}$ couple, just before the onset of a catalytic water oxidation wave. There appears to be significant base-assisted enhancement of the water oxidation wave, as can be inferred from the increase in catalytic current when going from H_2O to H_2PO_4^- to HPO_4^{2-} as the dominant proton acceptors at pH 1.0, 2.9, and 6.5, respectively. This result is consistent with a proton-transfer event in the rate-limiting step.

Figure 3 (inset) shows the $E_{1/2}$ versus pH plot (Pourbaix diagram) for the $\text{Ru}^{\text{III/II}}$ and $\text{Ru}^{\text{IV/III}}$ couples for $[\text{Ru}^{\text{II}}(\text{bpaH}_2)(\text{pic})_2]$ (see Figures S12a and S12b for the Pourbaix diagrams for $[\text{Ru}^{\text{II}}(\text{bpaH}_2)(\text{pic})_2]$ and $[\text{Ru}^{\text{II}}(\text{bpaH}_2)(\text{isq})_2]$, respectively). Three distinct regions are observed for the $\text{Ru}^{\text{III/II}}$ couple for $[\text{Ru}^{\text{II}}(\text{bpaH}_2)(\text{pic})_2]$, with slopes of -30 mV per pH unit (pH 0–1.3), -90 mV per pH unit (pH 1.3–4.5), and 0 mV per pH unit (pH > 4.5). This unusual behavior can be explained in terms of Equations (1)–(5) and calculated $\text{p}K_a$ values for the different species involved (see Table S3). From pH 0 to 1.3, the observed slope of -30 mV per pH unit is the average of the two slopes given by Equation (1) (0 mV per pH unit) and Equation (2) (-60 mV per pH unit) as a result of indistinguishable $\text{p}K_a$ values for $[\text{Ru}^{\text{III}}(\text{bpaH}_2)(\text{pic})_2]^+$ (0.5, DFT) and $[\text{Ru}^{\text{III}}(\text{bpaH})(\text{pic})_2]$ (1.8, DFT), with an observable single average $\text{p}K_a$ value of 1.3 for $[\text{Ru}^{\text{III}}(\text{bpaH}_2)(\text{pic})_2]^+$. Similarly, from pH 1.3 to 4.5, the observed slope of -90 mV per pH unit is the average of the two slopes given by Equation (3) (-120 mV per pH unit) and Equation (4) (-60 mV per pH unit) as a result of indistinguishable $\text{p}K_a$ values for $[\text{Ru}^{\text{II}}(\text{bpaH}_2)(\text{pic})_2]$ (3.6, DFT) and $[\text{Ru}^{\text{II}}(\text{bpaH})(\text{pic})_2]^-$ (4.2, DFT), with an observable single average $\text{p}K_a$ value of 4.5 for $[\text{Ru}^{\text{II}}(\text{bpaH}_2)(\text{pic})_2]$. A single, average $\text{p}K_a$ value for $[\text{Ru}^{\text{II}}(\text{bpaH}_2)(\text{pic})_2]$ of approximately 4.5 was also observed by absorption spectroscopy (see Figure S13). Finally, above pH 4.5, the redox process is described by Equation (5) and becomes pH-independent, consistent with the results in Figure 3. $[\text{Ru}^{\text{II}}(\text{bpaH}_2)(\text{isq})_2]$ shows similar behavior, with $\text{p}K_a([\text{Ru}^{\text{III}}(\text{bpaH}_2)(\text{isq})_2]^+) = 1.0$ and $\text{p}K_a([\text{Ru}^{\text{II}}(\text{bpaH}_2)(\text{isq})_2]) = 4.5$ (see Figure S12B).



Another interesting feature of the $\text{Ru}^{\text{III/II}}$ couple for $[\text{Ru}^{\text{II}}(\text{bpaH}_2)(\text{pic})_2]$ in the pH 1.3–4.5 region is the decrease in

overall charge upon oxidation from $[\text{Ru}^{\text{II}}(\text{bpaH}_2)(\text{pic})_2]$ to $[\text{Ru}^{\text{III}}(\text{bpa})(\text{pic})_2]^-$, thus resulting in a negatively charged complex. To the best of our knowledge, such behavior has not been observed previously. The oxidation of Ru^{II} to Ru^{III} results in increased acidity of the phosphonic acid groups owing to their direct coordination to the Ru center. Furthermore, the dominant species over a wide range of pH values for all high oxidation states of these complexes are either neutral or negatively charged.

The oxidation of Ru^{III} to Ru^{IV} for $[\text{Ru}^{\text{III}}(\text{bpa})(\text{L})_2]^-$ is pH-independent above pH 1.3, with $E_{1/2} = +1.57$ and 1.60 V for $[\text{Ru}^{\text{III}}(\text{bpa})(\text{pic})_2]^-$ and $[\text{Ru}^{\text{III}}(\text{bpa})(\text{isq})_2]^-$, respectively (see Figure S12). This result is consistent with one-electron oxidation of $[\text{Ru}^{\text{III}}(\text{bpa})(\text{L})_2]^-$ to $[\text{Ru}^{\text{IV}}(\text{bpa})(\text{L})_2]$. From DFT calculations, the $E_{1/2}$ value for this couple is predicted at 1.41 V for $[\text{Ru}^{\text{III}}(\text{bpa})(\text{pic})_2]^-$, in reasonable agreement with the experiment. For this complex, the $E_{1/2}$ value for the $\text{Ru}^{\text{IV/III}}$ couple increases with a slope of 90 mV per pH unit as the pH decreases below 1.3. This result is consistent with a similar behavior of the $\text{Ru}^{\text{IV/III}}$ couple below pH 1.3 to that of the $\text{Ru}^{\text{III/II}}$ couple between pH 1.3 and 4.5. Access to high oxidation Ru^{IV} without oxo formation is not common and is enabled for $[\text{Ru}^{\text{IV}}(\text{bpa})(\text{L})_2]$ by the high electron density provided to the Ru center by the phosphonate groups. For comparison, the $E_{1/2}$ value for the $\text{cis}-[\text{Ru}^{\text{IV}}(\text{bpy})_2\text{Cl}_2]^{2+}/\text{cis}-[\text{Ru}^{\text{III}}(\text{bpy})_2\text{Cl}_2]^+$ couple (1.95 V) is 1.66 V above that of the corresponding $\text{cis}-[\text{Ru}^{\text{III}}(\text{bpy})_2\text{Cl}_2]^+/\text{cis}-[\text{Ru}^{\text{II}}(\text{bpy})_2\text{Cl}_2]$ couple ($E_{1/2} = 0.29$ V; see Figure S14).

For water oxidation with molecular catalysts, the coordination of one or more water molecules to the metal center is required. In some Ru catalysts, a water molecule is already coordinated at the Ru^{II} state.^[4b,5] In others, water replaces one of the ligands upon oxidation of Ru^{II} to Ru^{III} ^[6] as a result of the enhanced affinity of Ru^{III} for water compared to Ru^{II} , as in $[\text{Ru}(\text{bda})(\text{L})_2]$ complexes.^[6] $[\text{Ru}^{\text{II}}(\text{bpaH}_2)(\text{L})_2]$ belongs to a new category in which water coordinates to the metal center at the Ru^{IV} state. This coordination is possible owing to the increase in the bite angle for Ru^{IV} (127.6°, DFT) as compared to Ru^{II} (111.9°) and Ru^{III} (115.9°), the ability of 16-electron Ru^{IV} to accept another electron pair, and the increased electrophilicity of the metal center upon oxidation from Ru^{III} to Ru^{IV} . The attack of water on Ru^{IV} (see Figure S15 for the reaction coordinate) is barrierless with $\Delta G^{\text{O}} = +4.3$ kcal mol⁻¹ for the generation of $[\text{Ru}^{\text{IV}}(\text{bpa})(\text{pic})_2(\text{OH}_2)]$ from $[\text{Ru}^{\text{IV}}(\text{bpa})(\text{pic})_2]$ and H_2O . Furthermore, the calculated $\text{p}K_a$ values for $[\text{Ru}^{\text{IV}}(\text{bpa})(\text{pic})_2(\text{OH}_2)]$ and $[\text{Ru}^{\text{IV}}(\text{bpa})(\text{pic})_2(\text{OH})]^-$ are 1.1 and 8.1, respectively, with $[\text{Ru}^{\text{IV}}(\text{bpa})(\text{pic})_2(\text{OH})]^-$ as the dominant form over a wide range of pH values. The ΔG^{O} value for the generation of $[\text{Ru}^{\text{IV}}(\text{bpa})(\text{pic})_2(\text{OH})]^- + \text{H}^+$ from $[\text{Ru}^{\text{IV}}(\text{bpa})(\text{pic})_2]$ and H_2O is +5.4 kcal mol⁻¹.

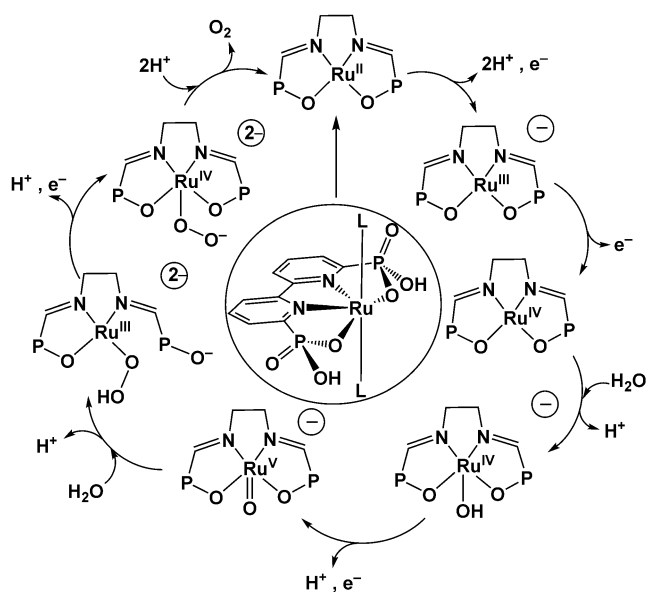
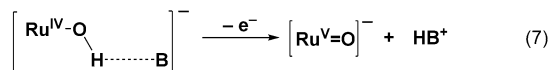
Initial studies showed that both $[\text{Ru}^{\text{II}}(\text{bpaH}_2)(\text{pic})_2]$ and $[\text{Ru}^{\text{II}}(\text{bpaH}_2)(\text{isq})_2]$ catalyze water oxidation to oxygen by Ce^{IV} in 0.1M HClO_4 and 0.1M HNO_3 (see Figure S16 for an evolved-oxygen versus time plot for $[\text{Ru}^{\text{II}}(\text{bpaH}_2)(\text{isq})_2]$). Kinetic studies are consistent with a rate-limiting step that is first-order in both catalyst and oxidant (see below). Spectral changes after the addition of 2.0 mM Ce^{IV} in 0.2M HNO_3 to aqueous solutions of $[\text{Ru}^{\text{II}}(\text{bpaH}_2)(\text{pic})_2]$ and $[\text{Ru}^{\text{II}}(\text{bpaH}_2)(\text{isq})_2]$

(*isq*)₂] are shown in Figure S17. For a range of catalyst concentrations, the data have been fitted to a single process, and plots of the observed first-order rate constants for the disappearance of Ce^{IV} were used to calculate overall rate constants, see Figure S18. The results are consistent with a rate-limiting oxidation step governed by the rate law in Equation (6), with $k_{\text{pic}} = (1.55 \pm 0.01) \times 10^3 \text{ M}^{-1} \text{ s}^{-1}$ and $k_{\text{isq}} = (1.92 \pm 0.03) \times 10^3 \text{ M}^{-1} \text{ s}^{-1}$. Turnover frequencies obtained from initial rates of Ce^{IV} consumption are 0.30 s⁻¹ for [Ru^{II}(bpaH₂)(pic)₂] and 0.40 s⁻¹ for [Ru^{II}(bpaH₂)(*isq*)₂], in good agreement with the initial turnover frequency of 0.15 s⁻¹ for [Ru^{II}(bpaH₂)(*isq*)₂] from the oxygen-evolution plot.

$$\frac{d[\text{Ce}^{\text{IV}}]}{dt} = k[\text{Ce}^{\text{IV}}][\text{Ru}] \quad (6)$$

It is difficult to obtain experimental redox potentials past Ru^{IV} owing to the electrocatalytic water oxidation wave. The proposed single-site mechanism for water oxidation by [Ru(bpaH₂)(L)₂] shown in Scheme 2 relies on DFT calculations for all intermediates past Ru^{IV}. The first step in the scheme is shown as a one-electron/2H⁺ step for simplicity, but it is more complex than that (see discussion of the Ru^{III/II} couple above).

The calculated $E_{1/2}$ value for the oxidation of [Ru^{IV}(bpa)(pic)₂(OH)]⁻ to [Ru^V(bpa)(pic)₂(OH)] is 1.46 V, just 50 mV past the calculated value for the Ru^{IV/III} couple at 1.41 V. This oxidation is facilitated by water coordination to Ru^{IV}, followed by deprotonation to generate electron-rich, seven-coordinate and 18-electron [Ru^{IV}-OH]⁻. Furthermore, the calculated pK_a value of [Ru^V(bpa)(pic)₂(OH)] is 0.4, and the generation of catalytically competent [Ru^V=O]⁻ is a PCET process [Eq. (7)].



Scheme 2. Proposed mechanism at pH 1.0.

These results are in full agreement with the experimental results: the onset of water oxidation catalysis is just past the Ru^{IV/III} couple, and there is significant base-assisted enhancement of the water oxidation wave with the involvement of a proton-transfer event in the rate-limiting step [Eq. (7)].

Once generated, [Ru^V=O]⁻ undergoes fast nucleophilic attack by a water molecule to generate [Ru^{III}-OOH]²⁻ in a process analogous to the atom-proton transfer (APT) observed in the O–O bond-formation step for other single-site catalysts.^[8] However, in this case the initial proton acceptor is one of the phosphonate groups of the bpa⁴⁻ ligand (see Figure S20), instead of a water molecule or an external base [Eq. (8)]; subsequent proton transfer to the bulk then occurs. This reaction results in a coordination contraction from seven-coordinate [Ru^V=O]⁻ to six-coordinate [Ru^{III}-OOH]²⁻ with decoordination of one of the phosphonate groups in the latter. Reaction coordinates for the key O–O bond-formation step, as well as the corresponding transition-state geometries, are shown in Figure S20 for both single-site ($\Delta G^{\ddagger} = +13.5 \text{ kcal mol}^{-1}$) and O–O coupling ($\Delta G^{\ddagger} = +31.9 \text{ kcal mol}^{-1}$) pathways. For [Ru^{II}(bda)(pic)₂], the ΔG^{\ddagger} value is +29.8 kcal mol⁻¹ for single-site O–O bond formation (see Figure S22). O–O bond formation for [Ru^{II}(bpaH₂)(pic)₂] is kinetically more favorable than both the corresponding single-site and radical coupling steps for [Ru^{II}(bda)(pic)₂].^[9] It is also kinetically more favorable than the O–O bond-formation step through radical coupling for [Ru^{II}(bpaH₂)(pic)₂]. This result clearly shows the special role of the phosphonate groups in reducing activation barriers to a point at which O–O bond formation is not rate-limiting.



The oxidation of ²[Ru^{III}-OOH]²⁻ to seven-coordinate ¹[Ru^{IV}-OOH]⁻ occurs at +0.60 V based on DFT calculations. The calculated pK_a value for ¹[Ru^{IV}-OOH]⁻ is 4.4, but once deprotonated the dominant species becomes ³[Ru^{IV}-OO]²⁻. The calculated pK_a value for the spin-forbidden acid–base equilibrium between ¹[Ru^{IV}-OOH]⁻ and ³[Ru^{IV}-OO]²⁻ is 2.2. Thus, deprotonation of ¹[Ru^{IV}-OOH]⁻ gives the intermediate ¹[Ru^{IV}-OO]²⁻ followed by intersystem crossing to generate the more stable intermediate ³[Ru^{IV}-OO]²⁻. Oxygen evolution is facile from ³[Ru^{IV}-OO]²⁻ and generates ³O₂ and ¹[Ru^{II}(bpa)(pic)₂]⁻, which undergoes protonation to ¹[Ru^{II}(bpaH₂)(pic)₂] to close the catalytic cycle (see Figure S23 for a reaction coordinate for facile O₂ evolution from ³[Ru^{IV}-OO]²⁻).

Bipyridyl diphosphonate ligands introduce multifunctionality in water oxidation catalysis. These systems allow access to high-valent metal–oxo species at mild potentials through redox-potential leveling due to charge compensation and σ -donation effects. Furthermore, the phosphonate groups act as proton shuttles to move protons in and out of the catalytic site, thus lowering activation barriers in PCET processes, particularly the key O–O bond-formation step. Finally, for bimolecular catalysts, such as [Ru(bda)(L)₂], the catalytic activity is significantly reduced on metal-oxide surfaces with site-isolated catalysts.^[6] For [Ru(bpaH₂)(L)₂] complexes, the catalytic activity is expected to remain unaltered on metal-

oxide surfaces as part of chromophore catalyst assemblies owing to their single-site nature. The incorporation of these catalysts in chromophore–catalyst assemblies is the subject of ongoing studies.

Experimental Section

Experimental procedures, computational details, and additional data are available in the Supporting Information. CCDC 1430167, 1430168, and 1430169 contain the supplementary crystallographic data for this paper. These data can be obtained free of charge from The Cambridge Crystallographic Data Centre.

Acknowledgements

This research was carried out at Brookhaven National Laboratory and supported by the U.S. Department of Energy, Office of Science, Division of Chemical Sciences, Geosciences, and Biosciences, Office of Basic Energy Sciences under contract DE-SC00112704.

Keywords: catalysis · electrochemistry · phosphonates · ruthenium · water splitting

How to cite: *Angew. Chem. Int. Ed.* **2016**, *55*, 8067–8071
Angew. Chem. **2016**, *128*, 8199–8203

- [1] a) N. Cox, D. A. Pantazis, F. Neese, W. Lubitz, *Acc. Chem. Res.* **2013**, *46*, 1588–1596; b) G. Renger in *Natural and Artificial Photosynthesis: Solar Power as an Energy Source (1)* (Ed.: R. Razeghifard), Wiley, Hoboken, **2013**, pp. 65–119; c) D. Shevela, L. O. Bjorn, Govindjee in *Natural and Artificial Photosynthesis: Solar Power as an Energy Source (1)* (Ed.: R. Razeghifard), Wiley, Hoboken, **2013**, pp. 13–63; d) D. J. Vinyard, G. M. Ananyev, G. C. Dismukes, *Annu. Rev. Biochem.* **2013**, *82*, 577–606; e) J. Yano, V. Yachandra, *Chem. Rev.* **2014**, *114*, 4175–4205.
- [2] a) S. W. Gersten, G. J. Samuels, T. J. Meyer, *J. Am. Chem. Soc.* **1982**, *104*, 4029–4030; b) F. Liu, J. J. Concepcion, J. W. Jurss, T. Cardolaccia, J. L. Templeton, T. J. Meyer, *Inorg. Chem.* **2008**, *47*, 1727–1752; c) I. López, S. Maji, J. Benet-Buchholz, A. Llobet, *Inorg. Chem.* **2015**, *54*, 658–666; d) A. C. Sander, S. Maji, L. Francas, T. Boehnisch, S. Dechert, A. Llobet, F. Meyer, *ChemSusChem* **2015**, *8*, 1697–1702; e) S. W. Sheehan, J. M. Thomsen, U. Hintermair, R. H. Crabtree, G. W. Brudvig, C. A. Schmuttenmaer, *Nat. Commun.* **2015**, *6*, 6469.
- [3] a) L. Duan, F. Bozoglian, S. Mandal, B. Stewart, T. Privalov, A. Llobet, L. Sun, *Nat. Chem.* **2012**, *4*, 418–423; b) L. Duan, A. Fischer, Y. Xu, L. Sun, *J. Am. Chem. Soc.* **2009**, *131*, 10397–10399; c) H.-W. Tseng, R. Zong, J. T. Muckerman, R. Thummel, *Inorg. Chem.* **2008**, *47*, 11763–11773.
- [4] a) Z. Chen, J. J. Concepcion, J. W. Jurss, T. J. Meyer, *J. Am. Chem. Soc.* **2009**, *131*, 15580–15581; b) J. J. Concepcion, J. W. Jurss, J. L. Templeton, T. J. Meyer, *J. Am. Chem. Soc.* **2008**, *130*, 16462–16463; c) J. J. Concepcion, M.-K. Tsai, J. T. Muckerman, T. J. Meyer, *J. Am. Chem. Soc.* **2010**, *132*, 1545–1557.
- [5] a) J. J. Concepcion, J. W. Jurss, M. R. Norris, Z. Chen, J. L. Templeton, T. J. Meyer, *Inorg. Chem.* **2010**, *49*, 1277–1279; b) D. J. Wasylenko, C. Ganesamoorthy, M. A. Henderson, B. D. Koivisto, H. D. Osthoff, C. P. Berlinguette, *J. Am. Chem. Soc.* **2010**, *132*, 16094–16106.
- [6] J. J. Concepcion, D. K. Zhong, D. J. Szalda, J. T. Muckerman, E. Fujita, *Chem. Commun.* **2015**, *51*, 4105–4108.
- [7] N. Song, J. J. Concepcion, R. A. Binstead, J. A. Rudd, A. K. Vannucci, C. J. Dares, M. K. Coggins, T. J. Meyer, *Proc. Natl. Acad. Sci. USA* **2015**, *112*, 4935–4940.
- [8] Z. Chen, J. J. Concepcion, X. Hu, W. Yang, P. G. Hoertz, T. J. Meyer, *Proc. Natl. Acad. Sci. USA* **2010**, *107*, 7225–7229.
- [9] J. Nyhlén, L. Duan, B. Åkermark, L. Sun, T. Privalov, *Angew. Chem. Int. Ed.* **2010**, *49*, 1773–1777; *Angew. Chem.* **2010**, *122*, 1817–1821.

Received: February 24, 2016

Revised: March 28, 2016

Published online: May 11, 2016